International Journal of Impact Engineering 38 (2011) 162–170

Contents lists available at ScienceDirect

International Journal of Impact Engineering

journal homepage: www.elsevier.com/locate/ijimpeng

Strain-rate effects on concrete behavior

Gianluca Cusatis*

Department of Civil and Environmental Engineering, Rensselaer Polytechnic Institute, Troy, NY 12180, USA

ARTICLE INFO

Article history:
Received 28 August 2009
Received in revised form
25 October 2010
Accepted 25 October 2010
Available online 11 November 2010

Keywords:
Concrete
Lattice models
Strain-rate effect
Creep
Concrete strength

ABSTRACT

In this paper, a previously developed meso-scale model for concrete, called the Confinement Shear Lattice (CSL) model, is extended in order to include the effect of loading rate on concrete strength and fracturing behavior. The rate dependence of concrete behavior is assumed to be caused by two different physical mechanisms. The first is a dependence of the fracture process on the rate of crack opening, and the second is the viscoelastic deformation of the intact (unfractured) cement paste. In this study, the first mechanism is described by the activation energy theory applied to the ruptures occurring along the crack surfaces, whereas the second mechanism is modeled by the Microprestress–Solidification theory. The developed model is calibrated and validated on the basis of experimental data gathered from the literature.

1. Introduction

Failure and fracturing behavior of concrete are very often treated as time-independent phenomena. This approach, however, is acceptable only as an approximation. In reality, the time dependence is negligible only in a certain range of load duration referred to as short term (or quasi-static) and pertaining to usual material testing lasting a few minutes. On the contrary, it is important for dynamic (impact) loading lasting a few milliseconds and for long-term (sustained) loading lasting for many years.

Under impact loading the influence of the loading rate on concrete behavior becomes an important parameter that must be taken into account in order to have reasonable results. It is generally reported that when the strain rate increases, the ultimate stress (strength), the elastic (secant) modulus, and the peak strain increase (see, among many others, Refs. [1,2]). Under sustained loading, on the other hand, viscoelastic deformations (creep) develop even at constant load and failure can occur at stress levels below the usual quasi-static strength [3].

To simulate correctly the dynamic and viscoelastic response of concrete structures with the inclusion of strain-rate effect, it is essential to adopt a computational model that simulates reliably the transition between diffuse damage, crack initiation, and crack propagation. Such a complex scenario is strongly influenced by concrete heterogeneity and it calls for the adoption of a meso-scale model in which heterogeneity is explicitly simulated.

Many meso-scale models can be found in the literature for the simulation of concrete behavior and, in particular, for the simulation of fracture propagation. Each of them has its own advantages and disadvantages. In the studies of Roelfstra et al. [4], Wittmann et al. [5] and, more recently, Carol et al. [6], concrete is modeled as a three-phase material (aggregate inclusions, mortar matrix, and interface between them), each phase being discretized through finite elements with appropriate material properties. These models describe with great accuracy the interaction between matrix and inclusions, but are almost prohibitive from a computational point of view. Lattice and particle models use a different approach in which the continuum is replaced by a system of discrete elements (rigid particles, truss members, beam members, etc.). Noteworthy examples of lattice and particle models can be found in Refs. [7–13]. These models can handle well the displacement discontinuity associated with fracture and they have been very successful in simulating tensile crack initiation and propagation in concrete.

In this study, a meso-scale model of concrete previously developed by the author is adopted and extended to include strain-rate effects. This model, called the Confinement–Shear Lattice model [14], is able to simulate tensile fracture as well as damage in compression and it has been extensively calibrated and validated in the quasi-static regime [15–17]. The quasi-static formulation of this model is highlighted in the next section.

* Tel.: +1 518 276 3956.
E-mail addresses: gianluca@cusatis.us, cusatg@rpi.edu.

0734-743X/$ – see front matter © 2010 Elsevier Ltd. All rights reserved.
doi:10.1016/j.ijimpeng.2010.10.030

2. Review of the Confinement–Shear Lattice (CSL) model

The Confinement–Shear Lattice (CSL) model is a meso-scale model simulating the mechanical interaction among coarse aggregate pieces in concrete. The geometry of the model is obtained from the basic properties of the mix-design. Given the aggregate–cement ratio, a/c, the cement content, c, the sieve curve, and a certain volume of material, V, the number n_i of aggregate pieces whose characteristic size lies in a specified size interval of average size D_i can be calculated: $n_i = \psi_i M_a/\rho_a v_i$, where $v_i = \pi D_i^3/6$ is the volume of one aggregate piece, ψ_i is the ratio between the mass of aggregate with characteristic size D_i and the total mass of aggregate, $M_a=(a/c)cV$, and ρ_a is the mass density of aggregate.

The aggregate pieces (particles), assumed to be of spherical shape, are randomly placed in the volume one-by-one through a try-and-reject procedure ensuring that each particle does not overlap with the other particles and is completely contained within the volume of interest [7]. The Delaunay algorithm [18] is then used to connect the centers of the particles through a three-dimensional lattice. Each ridge of the Delaunay tetrahedra identifies a lattice strut connecting two adjacent particles. The cross-sectional area of the lattice struts is defined such that the total volume of the struts corresponds to the considered volume of material (see Ref. [14] for more details).

Along each connecting strut, a point (interaction point), at which the forces between the two adjacent particles (of size D_1 and D_2) are imagined to be transmitted, is defined such that the strut length l is subdivided into two lengths $l_1 = lD_1/(D_1 + D_2)$ *and* $l_2 = lD_2/(D_1 + D_2)$ (Fig. 1a).

The kinematics of the model is defined assuming that: 1) the axial velocity, $\dot{u}$, is linearly distributed between the particle centers (lattice nodes), and 2) the transverse velocities $\dot{v}, \dot{w}$ are the effect of a rigid motion corresponding to the translational and rotational velocities at particle 1, for side $\overline{13}$, and at particle 2 for side $\overline{24}$ (see Fig. 1a). The transversal velocities at the interaction point can be then computed as $\dot{v}_3 = \dot{v}_1 + l_1\dot{\vartheta}_1$, $\dot{v}_4 = \dot{v}_2 - l_2\dot{\vartheta}_2$, $\dot{w}_3 = \dot{w}_1 - l_1\dot{\varphi}_1$ and $\dot{w}_4 = \dot{w}_2 + l_2\dot{\varphi}_2$, where $\dot{\varphi}$ and $\dot{\vartheta}$ are the rotational nodal velocities orthogonal to the axis of the lattice strut.

The velocity field is then used to define appropriate measures of strain rates at the interaction point: $\dot{\varepsilon}_N = (\dot{u}_2 - \dot{u}_1)/l$, $\dot{\varepsilon}_M = (\dot{v}_4 - \dot{v}_3)/l = (\dot{v}_2 - \dot{v}_1 - l_2\dot{\vartheta}_2 - l_1\dot{\vartheta}_1)/l$ and $\dot{\varepsilon}_l = (\dot{w}_4 - \dot{w}_3)/l = (\dot{w}_2 - \dot{w}_1 + l_2\dot{\varphi}_2 + l_1\varphi_1)/l$, where N is the direction coaxial with the connecting strut and M, L are two mutually orthogonal directions in the plane of the strut cross section.

Finally, the CSL formulation is completed by a constitutive relation characterizing the behavior of the particle interface at the interaction point. Following Ref. [14] normal and shear stresses, are assumed to be proportional to normal and shear strains through damage-like constitutive equations:

$$\sigma_N = \sigma\varepsilon_N/\varepsilon;\ \sigma_M = \sigma\alpha\varepsilon_M/\varepsilon;\ \sigma_L = \sigma\alpha\varepsilon_L/\varepsilon; \tag{1}$$

where $\sigma = \sqrt{(\sigma_N^2 + \sigma_T^2)/\alpha^2}$ = effective stress, $\sigma_T = \sqrt{\sigma_M^2 + \sigma_L^2}$ = shear stress, $\varepsilon = \sqrt{\varepsilon_N^2 + \alpha^2\varepsilon_T^2}$ = effective strain, and $\varepsilon_T = \sqrt{\varepsilon_M^2 + \varepsilon_L^2}$ = shear strain, and α is a material parameter discussed later.

The initial elastic behavior can be formulated through a linear elastic relationship between the effective stress and the effective strain: $\sigma = E_0\varepsilon$. In this case, from Eq. (1) one has $\sigma_N = E_0\varepsilon_N$, $\sigma_M = \alpha E_0\varepsilon_M$, *and* $\sigma_L = \alpha E_0\varepsilon_L$. As one can see the material parameter α represents the ratio between the shear elastic stiffness and the normal elastic stiffness. In Ref. [15] α was shown to control the macroscopic Poisson's ratio ν: for $\alpha = 0.25$ one obtains $\nu \approx 0.18$.

The elastic modulus E_0 must be computed preserving the different elastic properties of the aggregate pieces and the embedding mortar matrix. Assuming a series coupling, we have

$$E_0 = E_c l/(rl_a + l_c) \tag{2}$$

where E_c is the normal elastic modulus of the embedding mortar, $r = E_c/E_a$ is the ratio between the normal elastic moduli of the embedding mortar and aggregate, $l_a=(D_1 + D_2)/2$ *and* $l_c = l - l_a$.

The stress–strain evolution remains elastic as long as the effective stress σ does not reach a certain strength limit. Afterwards

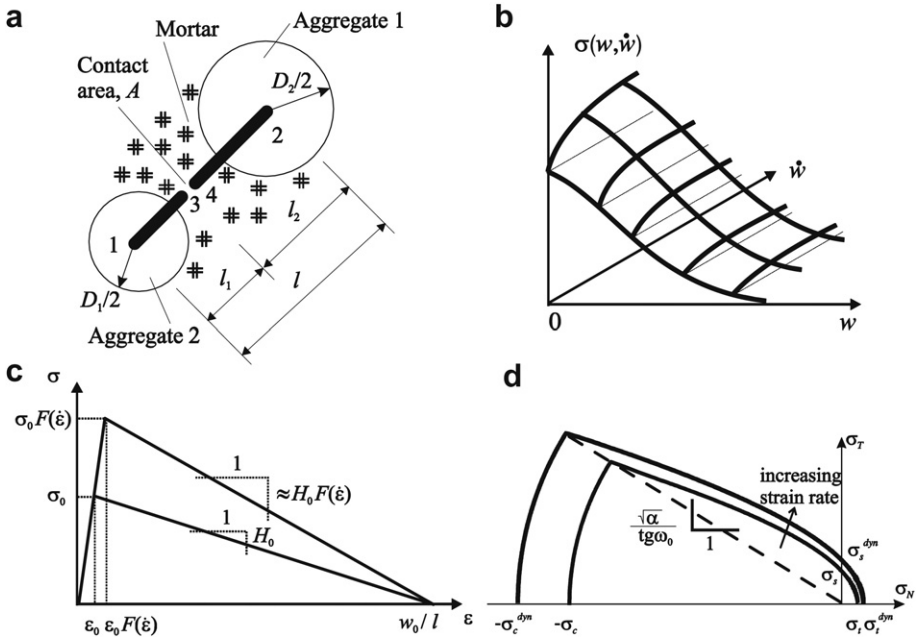

Fig. 1. a) Schematic representation of the lattice strut connecting two adjacent aggregate particles; b) Rate dependent cohesive law; c) Strain-rate dependent linear stress–strain law; d) CSL elastic domain and its rate dependence.

the evolution of the effective stress follows a given strain-dependent boundary. If unloading occurs, the behavior is considered to be incrementally elastic. The following equations govern the inelastic regime:

$$\dot{\sigma} = E_0\dot{\varepsilon} \text{ and } 0 \le \sigma \le \sigma_b(\varepsilon,\omega) \tag{3}$$

where ω, defined as $\tan\omega = \varepsilon_N/(\sqrt{\alpha}\varepsilon_T)$, represents a generalized strain measure characterizing the coupling between normal and shear behavior (pure shear for $\omega = 0$, pure tension for $\omega = \pi/2$, pure compression for $\omega = -\pi/2$, shear–tension coupling for $0<\omega<\pi/2$, and shear–compression coupling for $-\pi/2<\omega<0$). The constraint in Eq. (3) is imposed through a vertical (at constant strain) return algorithm. Similar approach was used in Refs. [19,20]. It must be noted that because of Eq. (1) the definition of ω can be rewritten in terms of stresses: $\tan\omega = \sqrt{\alpha}\sigma_N/\sigma_T$. This allows interpreting the strain-dependent boundary $\sigma_b(\varepsilon,\omega)$ as a strain-dependent limit domain in the stress space (σ_N,σ_T).

The strain-dependent boundary is defined by the equation

$$\sigma_b(\varepsilon,\omega) = \sigma_0(\omega)\ \exp\left\{\frac{K(\omega)\langle\varepsilon-\varepsilon_0(\omega)\rangle}{\sigma_0(\omega)}\right\} \tag{4}$$

where $\varepsilon_0(\omega) = \sigma_0(\omega)/E_0$.

The function $\sigma_0(\omega)$ is the effective strength limit and it represents the elastic domain in the stress space (σ_N,σ_T). In this work, the assumed elastic domain is a hyperbola with a cut-off in compression (Fig. 1d). The analytical expression of the hyperbolic portion is

$$\sigma_0(\omega) = \frac{-(\sigma_t+\sigma_a)s+\sqrt{[(\sigma_t+\sigma_a)s]^2+\left[\alpha(c/\mu)^2-s^2\right](\sigma_t+2\sigma_a)\sigma_t}}{\alpha(c/\mu)^2-s^2} \tag{5}$$

and the analytical expression of the compression cut-off reads

$$\sigma_0(\omega) = \frac{\sigma_c}{\sqrt{s^2+\alpha c^2/\beta}} \tag{6}$$

In the previous equations $s = \sin\omega$, $c = \cos\omega$, $\sigma_a = 0.5\sigma_t[\sigma_s^2/(\mu\sigma_t)^2 - 1]$, σ_t = meso-scale tensile strength, σ_s = meso-scale shear strength, σ_c = meso-scale compressive strength, μ = meso-scale friction coefficient, and β = compression cut-off shape parameter.

The function $K(\omega)$ represents the slope of the boundary $\sigma_b(\omega)$ (rate of strength decay) at the elastic limit $(\varepsilon = \varepsilon_0(\omega)$ or, equivalently, $\sigma = \sigma_0(\omega))$. In the case of pure meso-scale tension and shear, a softening behavior is assumed, $K(\pi/2) = -K_t < 0$ and $K(0) = -K_s/\alpha < 0$, while in the case of pure meso-scale compression, hardening behavior is assumed, $K(-\pi/2) = K_c > 0$ [14]. $K(\omega)$ is formulated as a linear interpolation of these three limiting cases. Unlike the hardening modulus K_c, the softening moduli K_t and K_s are not material parameters because they have to depend on the length l of the lattice element in order to preserve correct energy dissipation during softening [21]: $K_t = 2E_0/(l_t/l - 1)$ and $K_s = 2\alpha E_0/(l_s/l - 1)$ where $l_t = 2E_0G_t/\sigma_t^2$, $l_s = 2\alpha E_0G_s/\sigma_s^2$, G_t = meso-scale tensile fracture energy, and G_s = meso-scale shear fracture energy. Additional details on the CSL formulation can be found in Ref. [14].

3. Meso-level fracture as a time dependent phenomenon

Following the work of Bažant and coworkers [20], the rate dependence of concrete deformation can be assumed to be caused by two different physical mechanisms. The first is a dependence of the fracture process on the rate of crack opening, and the second is the viscoelastic deformation of cement paste. For concrete both mechanisms are important but the former dominates at extreme strain rates under impact. In addition, even for moderate strain rates, the rate dependence of fracture is needed to describe the reversal of softening into hardening after a sudden increase of the loading rate [3,22,23].

By considering fracture as a thermally activated phenomenon governed by the classical Maxwell–Boltzmann equation, Bažant [24] derived the dependence of the cohesive behavior on the crack opening rate as

$$\sigma_{ch}(w,\dot{w}) = \left[1 + c_1\operatorname{asinh}\left(\frac{\dot{w}}{c_0}\right)\right]f(w) \tag{7}$$

where σ_{ch} is the cohesive stress, w is the crack opening, $\dot{w}$ is the crack opening rate, $f(w)$ is the cohesive law under (ideal) static conditions ($\dot{w}\to 0$), and c_0, c_1 are two material parameters. The function $f(w)$ can be also considered a good approximation of a cohesive law identified in typical concrete fracture quasi-static tests in which the maximum crack opening rate is used as the control variable [24]. In these situations $\dot{w}$ is non zero but small and, consequently, $\sigma_{ch} \approx f(w)$. Eq. (7) represents a vertical scaling of the static cohesive law by a function of the crack opening rate as it is shown in Fig. 1b.

If one adopts a smeared crack approach at the meso-scale then one can consider the crack opening to be homogenously distributed along the connecting strut between two aggregate pieces. For the CSL model and with reference to the effective strains and stresses, one can write

$$\varepsilon = \frac{w}{l} + \frac{\sigma(w,\dot{w})}{E_0} \tag{8}$$

By solving Eq. (8) for w under the assumption that the elastic strain rate is negligible in comparison to the smeared crack opening rate during softening ($\dot{\varepsilon} = \dot{w}/l + \dot{\sigma}/E_0 \approx \dot{w}/l$), one can obtain the relationship between the crack opening and the effective strain and strain rate: $w = w(\varepsilon,\dot{\varepsilon})$. This relationship, in turn, allows obtaining the stress–strain relation $\sigma(\varepsilon,\dot{\varepsilon})$ from the cohesive law. For example, if the cohesive law is linear the stress–strain relationship is the one sketched in Fig. 1c. The peak stress and strain are given by the static ones times a function of the strain rate, $F(\dot{\varepsilon})$. The post-peak slope is $H = F(\dot{\varepsilon})\sigma_0/(w_0/l - \varepsilon_{\text{peak}})$ where $\varepsilon_{\text{peak}} = \varepsilon_0F(\dot{\varepsilon})$. Since $w_0/l >> \varepsilon_{peak}$ one can write $H \approx F(\dot{\varepsilon})\sigma_0/(w_0/l) = F(\dot{\varepsilon})H_0$, where $H_0 = \sigma_0 l/w_0$ is the post-peak slope under static condition.

According to the discussion above, the CSL boundary in Eq. (4) can be modified as

$$\sigma_b(\varepsilon,\dot{\varepsilon},\omega) = F(\dot{\varepsilon})\sigma_0(\omega)\ \exp\left\{\frac{K(\omega)\langle\varepsilon-\varepsilon_0(\dot{\varepsilon},\omega)\rangle}{\sigma_0(\omega)}\right\} \tag{9}$$

where $\varepsilon_0(\omega,\dot{\varepsilon}) = F(\dot{\varepsilon})\sigma_0(\omega)/E_0$. The function $F(\dot{\varepsilon})$ follows from Eq. (7) in which $\dot{w}$ is substituted by $l\dot{\varepsilon}$:

$$F(\dot{\varepsilon}) = \left[1 + c_1\operatorname{asinh}\left(\frac{\dot{\varepsilon}}{c_0/l}\right)\right] \tag{10}$$

Fig. 1b shows the variation of the elastic domain for increasing strain rate.

In the previous equations the strain-rate dependent function $F(\dot{\varepsilon})$ does not depend on the coupling variable ω. This means that in the current formulation the strength increment due to rate effect is the same for meso-scale tension, meso-scale shear, and meso-scale compression. This is somewhat arguable since the meso-scale compressive behavior in the CSL formulation governs mainly the macroscopic triaxial compressive behavior which is known [25,26] to be much less strain-rate sensitive than macroscopic tensile

fracturing and macroscopic unconfined compressive behavior (both governed by meso-scale tensile fracturing and shearing). However, in this paper simulation of triaxial behavior is not being investigated and will be the subject of future studies.

4. Incorporation of creep

Although the focus of this paper is to study the effect of high strain rates on concrete strength for which creep effects are secondary, in this section, for the sake of generality, a comprehensive theory that incorporates the aging viscoelasticity is amalgamated with the CSL model.

Assuming the additivity of the strains, each CSL strain component can be expressed as

$$\varepsilon_i = \xi_i + e_i \ (i = N, M, L) \tag{11}$$

where ξ_i includes the elastic strain of the aggregate, the instantaneous (elastic) strain of the embedding mortar and the damage (fracturing) strain. In general, the strain component e_i is the sum of the viscoelastic strain and the higro-thermal strains.

The evolution of ξ is assumed to be governed by the strain-rate dependent CSL formulation presented in the previous section. One can write

$$\dot{\sigma} = \dot{\xi}/q_1 \ \text{ and } \ 0 \le \sigma \le \sigma_b\left(\xi, \dot{\xi}, \gamma\right) \tag{12}$$

$$\sigma_N = \sigma\frac{\xi_N}{\xi}; \sigma_M = \sigma\frac{\alpha\xi_M}{\xi}; \sigma_L = \sigma\frac{\alpha\xi_L}{\xi} \tag{13}$$

$$\xi = \sqrt{\xi_N^2 + \alpha\xi_T^2}; \gamma = \arctan\left(\frac{\xi_N}{\sqrt{\alpha}\xi_T}\right); \sigma = \sqrt{\sigma_N^2 + \frac{\sigma_T^2}{\alpha}} \tag{14}$$

where $\xi_T = \sqrt{\xi_M^2 + \xi_L^2}$ and $\sigma_T = \sqrt{\sigma_M^2 + \sigma_L^2}$. The stress–strain boundary σ_b is given by the Eq. (9) in which ε, $\dot{\varepsilon}$ and ω are replaced by ξ, $\dot{\xi}$ and γ, respectively. The parameter q_1 is the CSL instantaneous (elastic) compliance that includes the instantaneous compliance of aggregate and embedding mortar. According to the series coupling assumption already used in the previous sections, one can write

$$q_1 = \frac{l_a/E_a + l_c q_{1,c}}{l} \tag{15}$$

where E_a is the elastic modulus of the aggregate, $q_{1,c}$ is the instantaneous and time-independent compliance of the embedding mortar. It must be noted here that the compliance $q_{1,c}$ does not correspond to the inverse of the elastic modulus E_c in Eq. (2); E_c is the quasi-static elastic modulus which, contrarily to $q_{1,c}$, includes the effect of short-term creep. Rather, $q_{1,c}$ should be interpreted as an ideal compliance that one would measure conducting a test at infinite strain rate and, as such, it can be considered to be approximated by the dynamic compliance of the embedding mortar. The reader is directed to Ref. [28] for an in depth discussion of this issue.

The strain components e_i are assumed to evolve according to the Micropretress–Solidification (MS) theory which is highlighted below. The comprehensive description of this theory along with its calibration and validation is reported elsewhere [29].

The MS theory assumes that $e_i = \varepsilon_i^{ev} + \varepsilon_i^f + \varepsilon_i^{sh} + \varepsilon_i^T$ in which ε_i^{ev} is the viscoelastic strain, ε_i^f is the purely viscous strain, and ε_i^{sh}, ε^T are the strains related to variations of humidity (shrinkage and swelling) and temperature, respectively. The hygro-thermal phenomena governing ε_i^{sh} and ε_i^T [29] are slow processes (at least for temperatures less than 100 °C) and are only relevant to the behavior of concrete subjected to sustained loads and will not be considered hereinafter.

The viscoelastic strain ε_i^{ev} takes into account the viscoelastic behavior of the CSH–gel particles. According to the Solidification theory [30] this component of the strain can be expressed in incremental form as (for $i = N,M,L$)

$$\dot{\varepsilon}_i^{ev}(t) = \frac{l_c}{l}\frac{\dot{\gamma}_i(t)}{v(t_e)}; \frac{1}{v(t)} = \frac{q_3}{q_2} + \left(\frac{\lambda_0}{t}\right)^m \tag{16}$$

$$\gamma_i(t) = \int_0^t \Phi_i(t_r(t) - t_r(\tau))\dot{\sigma}_i(\tau)\mathrm{d}\tau \tag{17}$$

$$\Phi_N = q_2 \ \ln\left[1 + \left(\frac{t - t'}{\lambda_0}\right)^n\right]; \Phi_M = \Phi_L = \frac{\Phi_N}{\alpha} \tag{18}$$

The function Φ_N is the non-aging micro-compliance function for the normal CSL strain components. The micro-compliance functions for the shear strain components Φ_M and Φ_L are assumed to be proportional to Φ_N by the factor $1/\alpha$ where α is the parameter introduced earlier to define the effective strain. This assumption implies, as it is usually accepted [30], that the Poisson's ratio is a time-independent parameter. The function v(t) describes the amount of solidified material during hydration processes, t_e is the equivalent time, and t_r is the reduced time as defined in Ref. [29]. The free parameters of the model are q_2 ($[q_2] = \text{M Pa}^{-1}$) and q_3 ($[q_3] = \text{M Pa}^{-1}$) while the others are fixed parameters with the following values $n = 0.1$, $\lambda_0 = 1$day, and $m = 0.5$. The ratio l_c/l in Eq. (16) is due to the fact that viscoelastic strains occur only in the embedding mortar which is distributed along the lattice length l_c.

The purely viscous strain (flow strain) is the completely irrecoverable part of the creep strain. In the Microprestress theory [29] the source of the flow component of creep is assumed to be the shear slips occurring along hindered adsorbed water layers between gel particles and it is modeled as

$$\dot{\varepsilon}_i^f(t) = \frac{l_c}{l}\frac{\psi_S}{\eta_i(S)}\sigma_i(t) \tag{19}$$

where ψ_S is the coefficient of reduced time that takes into account the effect of temperature and relative humidity [29] and the viscosities $\eta_i(S)$ are assumed to be proportional to the inverse of the microprestress S: $1/\eta_N(S) = k_0 q_4 S$, $\eta_M = \eta_L = \alpha\eta_N = 2\alpha k_0 q_4 S$. The microprestress S is an average of tensile stresses which are present across the slip planes represented by the hindered adsorbed water layers between the gel particles in the microstructure of the cement paste. The evolution of the microprestress can be calculated as follows [29]

$$\dot{S} + \psi_S k_0 S^2 = k_1\left|\dot{T} \ \ln(h) + T\frac{\dot{h}}{h}\right| \tag{20}$$

The free parameters of the Microprestress theory are q_4 ($[q_4] = \text{MPa}^{-1}$), k_0 ($[k_0] = \text{MPa}^{-1}\ \text{day}^{-1}$) and k_1 ($[k_1] = \text{MPa K}^{-1}$).

For stationary hygro-thermal conditions ($\dot{T} = 0$ and $\dot{h} = 0$) and full saturation ($h = 1$), the solution of Eq. (20) is $S(t) = (k_0 t)^{-1}$ [29].

5. Simplified creep formulation for short-duration dynamic events

The theory obtained by the amalgamation of the strain-rate dependent CSL model and the MS theory highlighted in the previous section is very sophisticated and accurate and it can model strain-rate effects in a wide range of loading durations. However,

the iterative algorithm needed to solve numerically the constitutive equations (computation of stresses for given total strains) is very demanding from a computational point of view [31]. For short-duration events, such as penetration and blast loading as well as earthquakes, the entire framework can be simplified.

It is reasonable to assume [20,32] that during a dynamic event: 1) microprestresses do not vary in time; 2) evolution of aging is negligible; 3) the viscoelastic strains are small compared to the damage strain $\xi_i = \varepsilon_i - \varepsilon_i^{ev} - \varepsilon_i^f \approx \varepsilon_i$. Under these assumptions it can be shown [20] that the MS theory is equivalent to a simple Maxwell-type rheological model where the incremental visco-elastic properties E_c^*, and η_c^* are obtained by requiring the compliance function of the Maxwell model to be tangent to the actual MS compliance function $J(t,t')$ (which can be obtained analytically, see Refs. [27,28]) at the time $t_{ch} = t_{load}/2$ where t_{load} = duration of the dynamic event. One obtains $E_c^* = 1/(J_{ch} - t_{ch}\dot{J}_{ch})$, $\eta_c^* = 1/\dot{J}_{ch}$, and $J_{ch} = J(t' + t_{ch}, t')$, $\dot{J}_{ch} = \dot{J}(t' + t_{ch}, t')$, *and* t' = age at loading.

In this case, the evolution of the effective stress can be calculated by simply substituting Eq. (12) by

$$(\dot{\sigma} + \sigma)/\tau = E\dot{\varepsilon} \text{ and } 0 \le \sigma \le \sigma_b(\varepsilon, \dot{\varepsilon}, \omega) \tag{21}$$

where $\tau = \eta/E$ is the relaxation time, $E = l/(l_a/E_a + l_c/E_c^*)$, and $\eta = l\eta_c^*/l_c$ [32].

6. Strain-rate effect on compressive and tensile strength

This section deals with the analysis of strain-rate effect on the macroscopic strength of concrete with reference to the experimental data by Dilger [33] who tested prismatic specimens (60 mm × 60 mm × 240 mm) in compression at three different nominal strain rates (3.3×10^{-5}, 3.3×10^{-3}, and 2.0×10^{-1} s^{-1}). In both the experiments and the numerical simulations, the specimens were fixed at one end and loaded longitudinally through an applied constant velocity at the other end. It must pointed out here that, the nominal strain rates reported above are defined as the applied velocity divided by the length of the specimens, and, as such, they only represent a global measure of the loading rate. Strain and strain-rate distributions throughout the specimens are clearly not uniform due to the dynamic character of the test, the effect of material heterogeneity, and triaxial boundary effects. These sources of non-uniformity of the response are all captured by the numerical meso-scale simulations.

The tested concrete was characterized by the following material properties: a/c = 5.5, $c = 320$ kg/m^3, $\rho_a = 2880$ kg/m^3, and a quasi-static design strength of about 22 MPa. Table 1 reports the granulometric distribution of the mix-design. The specimens were tested 28 days after casting. The fitting of the experimental data through the CSL model was obtained by setting the model parameters to the following values: $\alpha = 0.25$, $E_a = 300{,}000$ MPa, $\sigma_t = 6$ MPa, $G_t = 0.04$ N/mm, $\sigma_c = 13\sigma_t$, $K_c = 0.01E_c^*$, $\sigma_s = 3\sigma_t$, $\mu = 0.6$, $c_0 = 1 \times 10^{-5}$ s^{-1}, $c_1 = 5 \times 10^{-2}$, $q_1 = 1.7 \times 10^{-5}$ MPa^{-1}, $q_2 = 3.2 \times 10^{-5}$, MPa^{-1}, $q_2 = 0.9 \times 10^{-6}$M Pa^{-1}, and $q_4 = 3.5 \times 10^{-6}$ MPa^{-1}. The parameters E_c^* and η_c^* (see Section 5) were computed by considering the following loading durations: 180, 1.8 and 0.03 s, respectively, for the three different strain rates.

Fig. 2a reports the comparison between the numerical results (solid curves) and the experimental data (symbols) in terms of nominal stress (applied forces divided by the specimen cross-sectional area) versus nominal strain (calculated with a measure length = 160 mm in the central part of the specimens) curves and the agreement is very good. It must be noted here that the calibration of the parameters c_0 and c_1 (governing the strain-rate effect at the meso-scale, see Section 3) was obtained on the basis of only two strain rates (3.3×10^{-5}, and 3.3×10^{-3} s^{-1}). Consequently, the simulation of the third available strain rate (2.0×10^{-1} s^{-1}) can be regarded as a validation of the ability of the model to predict concrete strength outside the range of strain rates used for calibration.

In Fig. 2a, the experimental data points are relevant to the force measured at the moving end of the specimens. The numerical simulations (solid curves), on the other hand, are actually the plot of two curves relevant to the nominal stress computed at the moving (σ_A) and fixed (σ_R) end of the specimens (see also Fig. 2b). Due to the dynamic character of the test, at any given time σ_A and σ_R are not exactly equal and their difference can be visualized as the effect of longitudinal inertia forces distributed throughout the specimen. The fact that, for each of the considered strain rates, the two curves are indistinguishable suggests that inertia forces acting in the direction of the applied load are negligible. Based on this observation, can the experimental data points considered representative of the actual material behavior and not influenced by the structural features of the response? Not quite.

This issue is investigated in Fig. 2b where the response of the model relevant to a nominal strain rate of 0.5 s^{-1} is shown. In addition to σ_A and σ_R, the figure reports the response σ^* of the model in absence of inertial effects (static simulations) but including the strain-rate dependence of the material behavior. In this case, σ_A and σ_R are still almost coincident but both significantly differ from σ^*. The difference is due to the effect of inertia in the transverse direction (orthogonal to the applied load). Such an effect is a direct consequence of the lateral expansion occurring during the loading process and it can be regarded as the action of transverse inertia forces providing a certain degree of confinement. This confinement influences significantly both the peak stress and the post-peak response which, consequently, cannot be considered representative of the intrinsic material behavior. It must be noted here that the strain rates considered in this section are low to moderate. Of course the effect of inertia would be even more significant for high and very high strain rates.

Fig. 2c shows the comparison between the calculated and experimental compressive dynamic increase factor (DIF) defined as the ratio between the dynamic compressive strength and the quasi-static compressive strength. Experimental data includes the data used to calibrate the model as well as several other data sets gathered from the literature [34]. Numerical results are relevant to the peak stresses of the stress–strain curves computed at the moving end of the specimens, which include the effect of inertia forces (solid line with solid circles), and by static simulations, thus neglecting the inertia forces (solid line with triangles). The numerical results that include the effect of inertia forces fit well the experimental data in the entire range of strain rates (10^{-6}–10^{1} s^{-1}). The numerical results without inertia effects, however, underestimate the DIF for strain rates higher than 10^{-1} s^{-1}. This suggests that in this strain rate range the DIF data includes the effect of inertia and it should be considered a structural property, rather than a material property. An important consequence of this result is that the common practice of calibrating constitutive models by directly fitting DIF experimental data is not justified and the fitting should be based on the actual dynamic simulation of the tests used in the experiments. The situation is somehow different in the case of experimental data obtained through the Hopkinson bar technique [35]. In this case

Table 1
Granulometric distribution used in calculations.

	Size 1	Size 2	Size 3	Size 4	Size 5	Size 6
Diameter, D_i in mm	16	10	8	7	5	4
Amount, % in mass	12	12	7	7	6	7

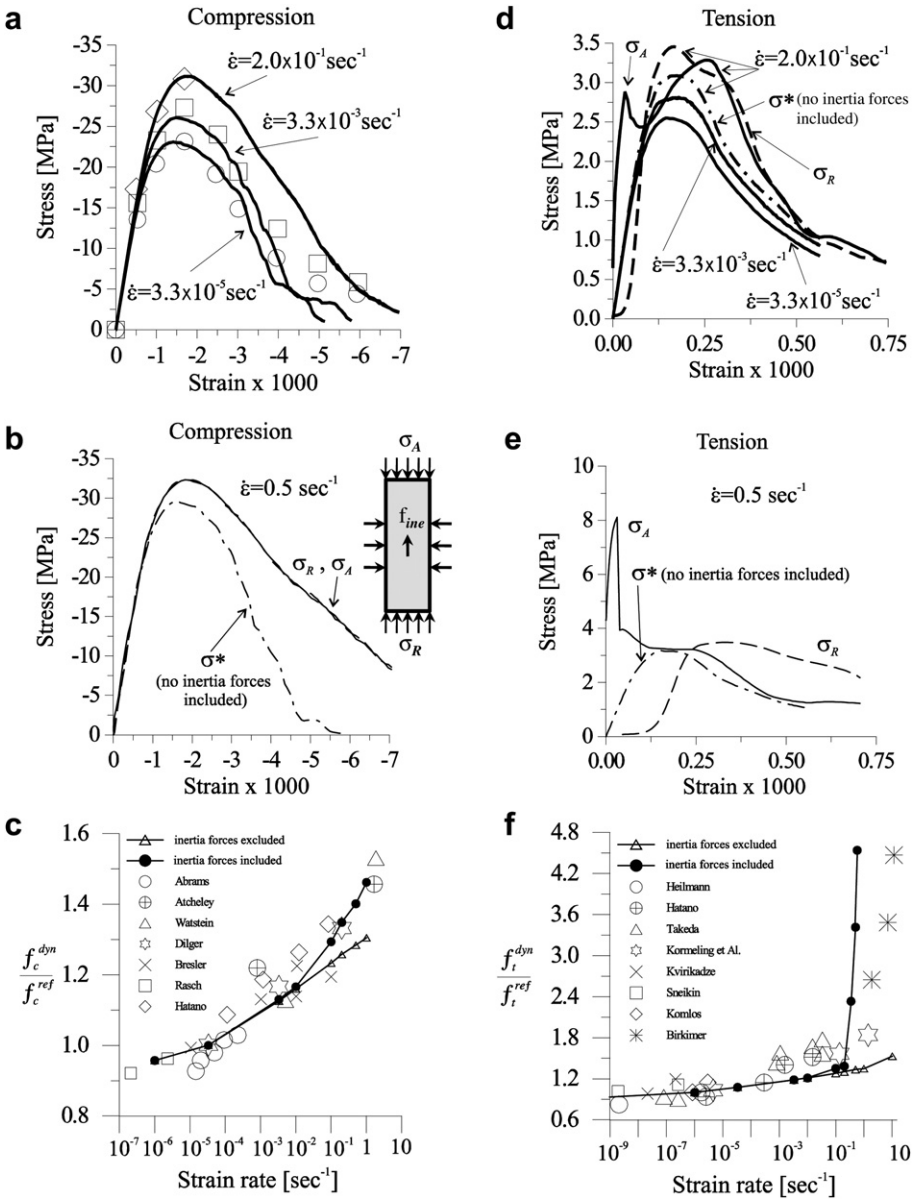

Fig. 2. a) Comparison between experimental data and numerical results for uniaxial compression; b) Tensile stress–strain curves at various strain rates; c) Inertia effect for compression simulation results; d) Inertia effect for tension simulation results; e) Compressive DIF; f) Tensile DIF.

a stress wave is let to propagate in the testing apparatus composed of an elastic incident bar, the specimen being tested, and an elastic transmitting bar. Comparison between strain measurements in the incident and transmitting bars provide the means to investigate material failure during a dynamic event. Clearly, the information that one can gather from the Hopkinson bar test is richer than the one obtained with the simple uniaxial test analyzed above. Nevertheless, it is still crucial to analyze the experimental results with the proper theory so that the material behavior is separated from the structural features of the specimen response. This can only be done with the accurate numerical simulation of the testing apparatus including detailed modeling of the specimen being tested as well as the interaction between the elastic bars and the specimens. For example, if the test is in compression it is important to simulate correctly frictional forces (which tend to confine the tested specimen) developing at the contact surfaces between the elastic bars and the tested specimens [36].

The issue discussed above is further investigated with reference to the tensile behavior. By using the same model parameters and test set-up used in the compression simulations, direct tension simulations were performed and the results are reported in Fig. 2d–f. Fig. 2d shows the obtained response for nominal strain rates equal to $3.3 \times 10^{-5}\ s^{-1}$, $3.3 \times 10^{-3}\ s^{-1}$ and $2 \times 10^{-1}\ s^{-1}$. For the lowest strain rates ($\propto 10^{-5}, 10^{-3}$) the nominal stress σ_A at the moving specimen end, the nominal stress σ_R at the fixed specimen end, and the response σ^* computed without inertia force basically coincide. For the highest strain rate ($2 \times 10^{-1}\ s^{-1}$) the effect of inertia forces is significant and σ_A, σ_R, and σ^* are distinctly different. However, the peak stress is not much different for the three curves. Fig. 2e shows the computed response in tension for a strain rate of $0.5\ s^{-1}$. In this case the inertia effect plays a non negligible role even for the nominal peak stress. The nominal peak stress σ_A at the moving specimen end is approximately twice the nominal peak stress σ_R at the fixed specimen end. The latter, in turn, is very close

to the nominal peak stress of the response σ^* obtained neglecting the effect of inertia. It must be noted here that σ_A is typically recorded in experiments and information about σ_R is usually not available. Finally, in Fig. 2f one can see the tensile DIF calculated with and without the effect of inertia forces and compared with experimental data gathered from the literature [34]. Once again, the effect of inertia, which is essentially a structural feature of the response, cannot be neglected to calculate correctly the DIF in the entire range of analyzed strain rates (10^{-9}–10^{1} s^{-1}).

The tensile DIF calculated without the inertia effect has values comparable to the compressive one (from 1 to 1.4). This is consistent with the fact that, in the CSL framework, both macroscopic compressive and tensile softening behaviors are the results of the same meso-scale physical phenomena, which are meso-scale fracturing and shearing (and there is no softening postulated for meso-scale compression) [14]. On the other hand the Dynamic Increase Factors calculated with the inertia effect (as well as the experimental ones) vary from 1 to 5 for tension, and from 1 to 1.6 for compression. This difference can be explained as follows. According to the discussion above one can write

$$-f_c^{dyn} = -f_c^* + f_c^{in};\ f_t^{dyn} = f_t^* + f_t^{in} \tag{22}$$

where f_c^{dyn}, f_t^{dyn} are the peaks of the nominal stresses at the moving specimen end; f_c^*, f_t^* are the peaks of the stress obtained neglecting inertia effects and f_c^{in}, f_t^{in} are the (structural dependent) contributions due to inertia effects. In an ideal situation in which the exact same test set-up and the same specimen is used for tension and compression, the accelerations in tension and compression have the same magnitude but opposite sign. Consequently, one can write

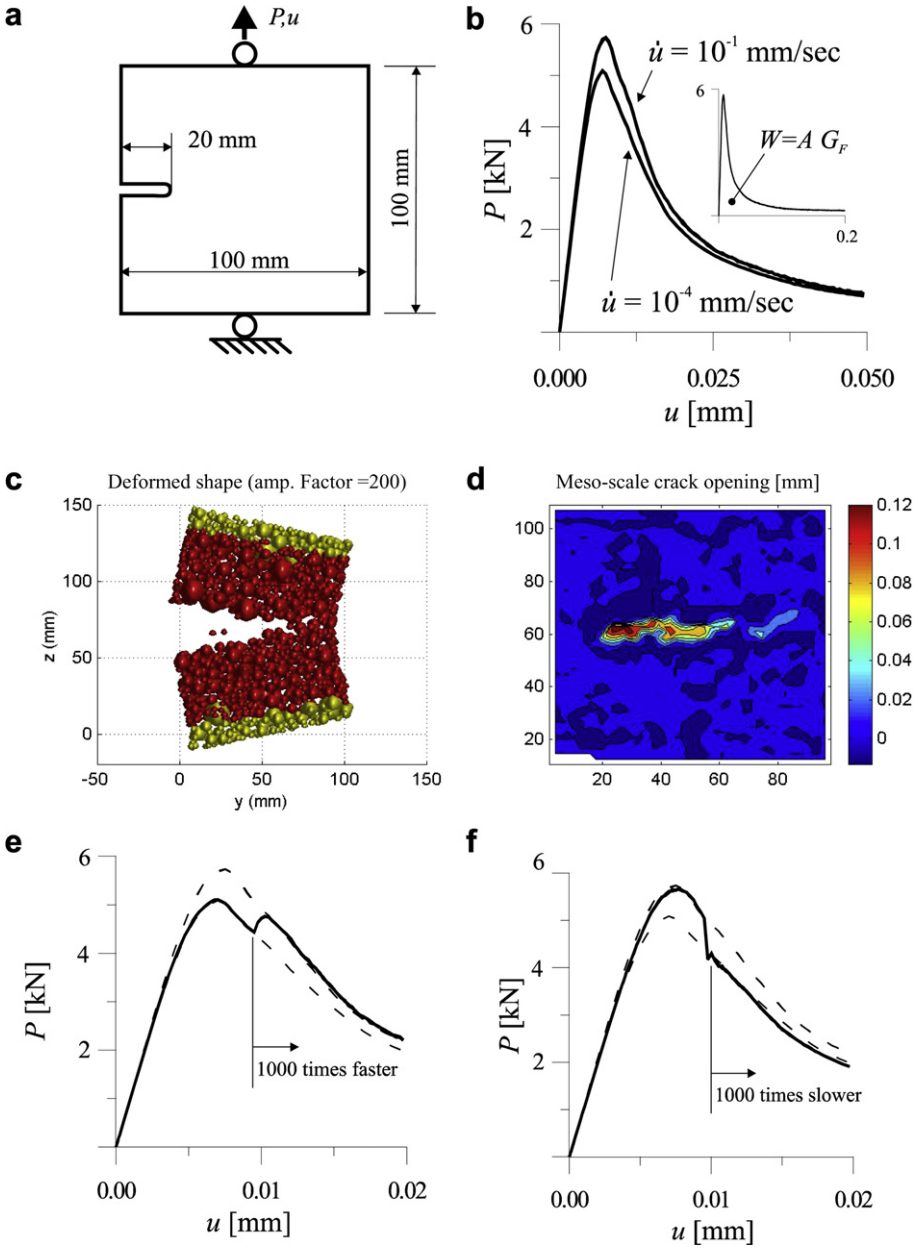

Fig. 3. a) Test set-up used for the simulations of fracture propagation; b) Load-displacement curves for two distinct loading rates; c) Amplified deformed shape at failure; d) Contours of meso-scale crack openings at failure; e) Fracturing response for a 1000-fold increase of the applied velocity; f) Fracturing response for a 1000-fold decrease of the applied velocity.

$f_c^{in} = -f_t^{in} = -f^{in}$. By exploiting this observation, dividing Eqs. (22) by the quasi-static strengths, and assuming the quasi-static tensile strength to be about one tenth of the compressive strength ($f_t' \approx f_c'/10$), one obtains

$$\mathrm{DIF}_c = \frac{f_c^{dyn}}{f_c'} = \mathrm{DIF}^* + \frac{f^{in}}{f_c'} \tag{23}$$

and

$$\mathrm{DIF}_t = \frac{f_t^{dyn}}{f_t'} = \mathrm{DIF}^* + \frac{f^{in}}{f_t'} \approx \mathrm{DIF}^* + 10\frac{f^{in}}{f_c'} \tag{24}$$

where DIF*, (assumed to be the same for tension and compression) is the DIF without the effect on inertia and representative of the intrinsic material behavior. The assumption that the intrinsic DIF* is the same for tension and compression is motivated by the fact that macroscopic tensile failure and macroscopic unconfined compressive failure are both the effect of meso-scale tensile fracturing and shearing. This aspect is correctly reproduced by the CSL formulation. By comparing Eqs. (23) and (24) it is evident that the contribution of the inertia forces to the tensile DIF is about ten times bigger than the contribution of the inertia forces to the compressive DIF.

7. Strain-rate effect on fracturing behavior

In addition to the strength, the rate of loading influences the fracturing behavior of concrete. In this section, this effect is discussed through the analysis of a single notched specimen subject to direct tension. The adopted geometry of the specimen and boundary conditions are reported in Fig. 3a. The specimen out-of-plane thickness is 40 mm. Concrete properties and the model parameters are the same used in the previous section.

Two different rates of loading are considered, $\dot{u} = 10^{-4}$ mm/sec and $\dot{u} = 10^{-1}$ mm/sec, where u is the displacement applied through a hinge-like boundary condition at the top side of the specimens. Fig. 3b shows the computed load-displacement curves for the two rates of loading. The peak load is obviously higher for the higher strain rate (5728 N compared to 5088 N). Calculation of the macroscopic fracture energy according to the work of fracture concept [37,38] (area under the load-displacement curve divided by the ligament area) provides an increase of the fracture energy (from 47.46 N/m to 52.05 N/m) as a function of the strain rate. This result is consistent with what is typically reported in the literature [3].

Fig. 3c and d report, for a load level in the far post-peak, the amplified (200 times) deformed shape and the contours of meso-scale crack opening, defined as $w = l[(\varepsilon_N - \sigma_N/E_N)^2 + (\varepsilon_T - \sigma_T/E_T)^2]^{1/2}$, respectively. As one can see, specimen failure is associated with a fracture propagating from the tip of the notch towards the opposite side of the specimen.

The previous results were obtained by constant loading rate. Nevertheless, it is interesting to examine the response of concrete under sudden changes (increase or decrease) of the loading rate. In Fig. 3e one can see the load-displacement curve obtained by a 1000-times increase of the loading rate during the post-peak. The post-peak softening reverses to post-peak hardening followed by a second peak. Afterwards the curve coincides with the monotonic curve for the higher rate of loading. The second peak may be higher or lower than the first peak at the previous slow rate of loading, depending on the ratio of rate increase and the magnitude of load decrease prior to the increase of loading rate. Fig. 3f shows the response related to a sudden decrease (1000 times) of the loading rate. In this case the slope of the load-displacement diagram suddenly becomes steeper. A milder slope is resumed when the load-displacement curve approaches the response for the lower loading rate. The obtained numerical results agree well with the experimental findings reported in Ref. [23]

8. Summary and conclusions

In this study the Confinement–Shear Lattice model, a meso-scale model for concrete, was extended to include the effect of strain rate on concrete mechanical behavior. This was achieved by incorporating into the CSL framework two key components: 1) the dependence of the cohesive law on the crack opening rate, and 2) the Microprestress–Solidification theory for concrete creep. The resulting model was calibrated and validated by comparison with experimental data relevant to uniaxial compression and uniaxial tension tests. In addition, numerical simulations of fracture propagation in notched specimens were carried out.

Based on the analysis of the results, the following observations on the proposed rate-dependent CSL model can be made.

1. The CSL model reproduces correctly the strain-rate dependence of compressive and tensile strength in a wide range of strain rates (from 10^{-9} to 10^{1} s^{-1}, see Fig. 2e,f).
2. In the CSL formulation, the same meso-scale mechanics is associated with macroscopic compressive failure and tensile failure. Consequently, the same intrinsic DIF is predicted by the model in tension and compression. Nevertheless, experimental data showing significant difference in the compressive and tensile DIF are fitted very well by the model if inertia effects (as well as other structural features of the tests such as specimen geometry and boundary conditions effects) are included in the numerical simulations.
3. The CSL model can simulate correctly strain-rate effects on concrete fracturing behavior. In particular, it can reproduce the material rehardening associated with a sudden increase of the loading rate.

More in general, the numerical simulations performed in this paper show that:

1. For strain rates higher than 10^{-1} s^{-1} the inertia forces cannot be neglected and provide a significant contribution to the strength enhancement recorded during experiments.
2. The common practice of calibrating constitutive laws by simply fitting the experimental dynamic increase factor (DIF) is not justified. Calibration should be performed through an inverse analysis based on the dynamic numerical simulation of the actual experiments (including their structural features) used to measure the DIF.
3. Due to the strength dissymmetry in tension and compression, inertia forces influence the tensile response much more than the compressive response.
4. By taking into account inertia effects, it seems not to be necessary (as customarily done) to consider two distinct Dynamic Increase Factors for compression and tension.

Acknowledgments

Financial support under DTRA grant HDTRA1-09-1-0029 to Rensselaer Polytechnic Institute and the editorial help of Dr. Ed Schauffert, post-doctoral research associate at Rensselaer Polytechnic Institute, are gratefully acknowledged.

References

[1] You JH, Hawkins NM, Kobayashi AS. Strain-rate sensitivity of concrete mechanical properties. ACI Mat J 1992;89(2):146–53.
[2] Watstein D. Effect of straining rate on the compressive strength and elastic properties of concrete. J Am Concrete Inst 1953;49(4):729–44.
[3] Bažant ZP, Gettu R. Rate effects and load relaxation: static fracture of concrete. ACI Mater J 1992;89(5):456–68.
[4] Roelfstra PE, Sadouki H, Wittmann FH. Le béton numérique. Mater Struct 1985;18:327–35.
[5] Wittmann FH, Roelfstra PE, Kamp CL. Drying of concrete: an application of the 3L-approach. Nucl Eng Des 1988;105:185–98.
[6] Carol I, Lopez CM, Roa O. Micromechanical analysis of quasi-brittle materials using fracture-based interface elements. Int J Num Method Eng 2001;52: 193–215.
[7] Bažant ZP, Tabarra MR, Kazemi T, Pijaudier-Cabot G. Random particle model for fracture of aggregate or fiber composites. J Eng Mech ASCE 1990;116 (8):1686–705.
[8] Schlangen E, van Mier JGM. Shear fracture in cementitious composites, Part II: numerical simualtions. In: Bažant ZP, editor. Fracture mechanics of concrete. New York: Elsevier; 1992.
[9] Schlangen E. Experimental and numerical analysis of fracture processes in concrete. PhD thesis, Delft University of Technology, Delft, The Netherlands, 1993.
[10] van Mier JGM, Vervuurt A, Schlangen E. Boundary and size effects in uniaxial tensile tests: a numerical and experimental study. In: Bažant ZP, Bittnar Z, Jirásek M, Mazars J, editors. Fracture and damage in quasibrittle structures. London: E & FN Spon; 1994.
[11] Schlangen E. Computational aspects of fracture simulations with lattice models. In: Wittmann FH, editor. Fracture mechanics of concrete structures. Freiburg, Germany: Aedificatio; 1995.
[12] Lilliu G, van Mier JGM. 3D lattice type fracture model for concrete. Eng Fracture Mech 2003;70:927–41.
[13] Yip M, Li Z, Liao B-S, Bolander JE. Irregular lattice models of fracture of multiphase particulate materials. Int J Fracture 2006;140(1–4):113–24.
[14] Cusatis G, Bažant ZP, Cedolin L. Confinement–shear lattice model for concrete damage in tension and compression: I. Theory. J Eng Mech ASCE 2003;129 (12):1439–48.
[15] Cusatis G, Bažant ZP, Cedolin L. Confinement–shear lattice model for concrete damage in tension and compression: II. Computation and validation. J Eng Mech ASCE 2003;129(12):1449–58.
[16] Cusatis G, Bažant ZP, Cedolin L. Confinement–shear lattice model for fracture propagation in concrete. Comput Methods Appl Mech Eng 2006;195:7154–71.
[17] Cusatis G, Cedolin L. Two-scale analysis of concrete fracturing behavior. Eng Fracture Mech 2006;74:3–17.
[18] Delaunay B. Sur la sphère vide. Bull Acad Sci USSR(VII) Classe Sci Mat Nat; 1934:793–800.
[19] Bažant ZP, Caner FC, Carol I, Adley MD, Akers SA. Microplane model M4 for concrete. I: formulation with work-conjugate deviatoric stress. J Eng Mech ASCE 2000;126(9):944–53.
[20] Bažant ZP, Caner FC, Adley MD, Akers SA. Fracturing rate effect and creep in microplane model for dynamics. J Eng Mech ASCE 2000;126(9):962–70.
[21] Bažant ZP, Oh BH. Crack band theory for fracture of concrete. Matériaux et Constructions 1983;16:155–77.
[22] Bažant ZP, Gu WH, Faber KT. Softening reversal and other effects of a change in loading rate on fracture of concrete. ACI Mat J 1995;92:3–9.
[23] Tandon S, Faber K, Bažant ZP, Li YN. Cohesive crack modeling of influence of sudden changes in loading rate on concrete fracture. Eng Fract Mech 1995;52:987–97.
[24] Bažant ZP. Creep and damage in concrete. In: Skanly J, Mindess S, editors. Materials science of concrete IV. Westerville, OH: Am Ceramic Soc; 1995.
[25] Lundeen RL. Dynamic and static tests of plain concrete specimens. Report 2. Phase 2: Flexure and triaxial compression. Technical Report. Vicksburg, MS, USA: US Army Engineer Waterways Experiment Station; 1964.
[26] Bažant ZP, Oh B-H. Strain-rate effect in rapid triaxial loading of concrete. J Engrg Mech Div ASCE 1982;108:764–82.
[27] Bažant ZP, Baweja S. Creep and shrinkage prediction model for analysis and design of concrete structures, model B3. Mater Struct 1995;28:357–65.
[28] Bažant ZP, Baweja S. Justification and refinement of model B3 for concrete creep and shrinkage: 1. Statistics and sensitivity. Mater Struct 1995;28: 415–30.
[29] Bažant ZP, Cusatis G, Cedolin L. Temperature effect on concrete creep modeled by microprestress–solidification theory. J Eng Mech ASCE 2004;130 (6):691–9.
[30] Bažant ZP, Prasannan S. Solidification theory for concretecreep. I: formulation. J Eng Mech ASCE 1989;115:1691–703.
[31] Cusatis G. Tridimensional particle model for concrete. Ph.D. Thesis, March 2002. Graduate School in Structural Engineering, Politecnico di Milano, Piazza Leonardo da Vinci 32, 20133, Milan, Italy.
[32] Cusatis G, Bažant ZP, Cedolin L. 3D lattice model for dynamic simulation of creep, fracturing and rate effect in concrete. In: Ulm FJ, Bažant ZP, Wittmann FH, editors. Proc Sixth Int Conf CONCREEP-6. Elsevier; 2001.
[33] Dilger WH, Koch R, Kowalczyk R. Ductility of plain and confined concrete under different strain rates. Am Conc Inst Spec Publ; 1978.
[34] Veerheijm J. Concrete under impact tensile loading and lateral compression. PhD thesis, Delft University of Technology, Prins Maurits Laboratorium TNO, 1992.
[35] Albertini C, Cadoni E, Labibes K. Impact fracture process and mechanical properties of plain concrete by means of an Hopkinson bar bundle. Proc 5th Int Congress on Mech and Phys Behaviour of materials under dynamic loading. J Phy IV 1997;7(3):915–20. Toledo, Spain.
[36] Cedolin L, Bianchi P, Cusatis G, Di Luzio G, Ratti A. Anchorages in normal and high performance concretes subjected to medium and high strain rates. Final Report, UE ANCHOR Project. Milan, Italy: Department of Structural Engineering, Politecnico di Milano University; March 2001.
[37] Hillerborg A. The theoretical basis of a method to determine the fracture energy G_F of concrete. Mater Struct 1985;18:29196.
[38] Hillerborg A. Results of three comparative test series for determining the fracture energy G_F of concrete. RILEM Tech Committee 1985;50. Fracture Mechanics of Concrete.